

Cite this: *RSC Adv.*, 2019, 9, 24280

Facile synthesis of few-layer MoS₂ in MgAl-LDH layers for enhanced visible-light photocatalytic activity

Guoyuan Zheng,^{ab} Caihong Wu,^{ab} Jilin Wang,^{*ab} Shuyi Mo,^{ab} Yanwu Wang,^c Zhengguang Zou,^{ab} Bing Zhou^{ab} and Fei Long^{ID *ab}

A new photocatalyst, few-layer MoS₂ grown in MgAl-LDH interlayers (MoS₂/MgAl-LDH), was prepared by a facile two-step hydrothermal synthesis. The structural and photocatalytic properties of the obtained material were characterized by several techniques including powder X-ray diffraction (XRD), Raman spectroscopy, field emission scanning electron microscopy (FESEM), high-resolution transmission electron microscopy (HRTEM), Fourier transform infrared spectroscopy (FTIR), X-ray photoelectron spectroscopy (XPS), photoluminescence spectroscopy (PL) and UV-vis absorption spectroscopy. The MoS₂/MgAl-LDH composite showed excellent photocatalytic performance for methyl orange (MO) degradation at low concentrations (50 mg L⁻¹ and 100 mg L⁻¹). Furthermore, even for a MO solution concentration as high as 200 mg L⁻¹, this composite also presented high degradation efficiency (>84%) and mineralization efficiency (>73%) at 120 min. The results show that the MoS₂/MgAl-LDH composite has great potential for application in wastewater treatment.

Received 22nd May 2019

Accepted 8th July 2019

DOI: 10.1039/c9ra03858b

rsc.li/rsc-advances

1. Introduction

Groundwater contamination due to dyes is still a serious environmental pollution problem, mainly because of the high toxicity and widespread use of dyes.^{1–4} Semiconductor photocatalytic degradation of organic pollutants in wastewater using inexhaustible and environmentally friendly solar energy has attracted much attention.^{5,6} TiO₂ is a commercially available semiconductor photocatalyst.^{21,24} However, it shows poor utilization of sunlight, due to the wide band gap of 3.2 eV which only absorbs sunlight with a wavelength of less than 420 nm. Therefore, researchers have been looking for other semiconductor photocatalysts as replacements for TiO₂.

As a typical graphene-like transition metal disulfide, MoS₂ is a potential photocatalyst.^{7–9,25} Unlike other semiconductor materials, based on the quantum confinement effect, the band gap of MoS₂ increases with the number of layers. Moreover, bulk MoS₂ is an indirect bandgap semiconductor with a band gap of 1.2 eV, and single-layer MoS₂ is a direct bandgap semiconductor with a band gap of 1.9 eV.¹⁰ It can be seen that single-

layer or few-layer MoS₂ is a potential photocatalytic semiconductor material. In addition, there are many unsaturated bonds and more active sites due to the complex edge structure of two-dimensional (2D) MoS₂. Therefore, preparation of single-layer or few-layer MoS₂ is particularly important for application in photocatalysis. For example, like for the preparation of graphene, single and few-layer MoS₂ have been prepared using mechanical exfoliation, the so-called “Scotch Tape Method”.¹¹ Obviously, the “Scotch Tape Method” is not a scalable process. Recently the Coleman group prepared a single-layer of MoS₂ by a surfactant-assisted sonication pioneering method.^{12–15} However, even if a single-layer of MoS₂ is prepared, the surface defects will lead to a high photoelectron-hole pair recombination efficiency, thus affecting the photocatalytic performance of MoS₂. Therefore, how to prepare single or few-layers of MoS₂ and inhibit the recombination of photoelectron-hole pairs is a challenging subject.

Based on the above reasons, we designed a single or few-layer MoS₂-intercalated layered double hydroxide (MoS₂/MgAl-LDH) composite as a novel photocatalyst. Few-layer MoS₂ can be obtained by the “space-confining” effect of the LDH interlayer. On the one hand, 2D MoS₂ can contribute more active sites. On the other hand, LDHs have excellent performance as carriers for photocatalyst composites. For example, Šárka *et al.* prepared ZnCr-CO₃ LDHs and derived mixed oxides that exhibited excellent adsorption and photocatalytic properties for Orange II.³⁵ Wu *et al.* prepared Cu₂O/ZnAl calcined layered double hydroxide (Cu₂O/ZnAl-CLDH) photocatalysts with superior photocatalytic activity.³³ Here we prepared MoS₂/MgAl-LDH

^aCollege of Materials Science and Engineering, Guangxi Key Laboratory of Optical and Electronic Materials and Devices, Guilin University of Technology, Guilin 541004, China. E-mail: longgf@glut.edu.cn; jilinwang@glut.edu.cn; Fax: +86 773 5896672; Tel: +86 773 5896700

^bGuilin University of Technology, Collaborative Innovation Center for Exploration of Hidden Nonferrous Metal Deposits and Development of New Materials in Guangxi, Guilin 541004, China

^cCollege of Environmental Science and Engineering, Guilin University of Technology, Guilin 541004, China



composites by hydrothermal synthesis, evaluated the catalytic performance of the catalyst by degrading methyl orange organic dyes, and conducted in-depth research on the synergistic mechanism of MoS₂ and MgAl-LDH.

2. Experimental

2.1. Synthesis of various materials

All reagents were analytical grade and used without further purification. MoS₂/MgAl-LDH was prepared by a simple two-step hydrothermal process. First, MgAl-LDH with MoO₄²⁻ intercalated in the interlayer (MoO₄²⁻/MgAl-LDH) was prepared by a hydrothermal method. During the synthesis process, Mg(NO₃)₂·6H₂O (4.615 g) and Al(NO₃)₃·9H₂O (3.376 g) with a M²⁺/M³⁺ molar ratio of 2.0/1.0 were dissolved in 50 mL degassed distilled water to form solution A. Then, NaOH (2.516 g) was dissolved in 25 mL degassed distilled water to produce solution B. Na₂MoO₄·2H₂O (7.561 g) was dissolved in 25 mL degassed distilled water to form solution C. Solutions A and B were added dropwise to a reaction vessel containing solution C with vigorous, constant stirring at a constant pH of 10 and at 60 °C. After the addition, the resultant slurry was cooled to room temperature and aged for 10 h at 140 °C. MoO₄²⁻/MgAl-LDH was washed several times with large amounts of deionized water and lyophilized in a vacuum freeze dryer.

Then, MoO₄²⁻/MgAl-LDH (0.5 g) and thiourea (0.38 g) were added to 60 mL degassed distilled water and stirred. After stirring, the resultant slurry was subsequently aged for 24 h at 205 °C. MoS₂/MgAl-LDH was washed several times with a large amount of deionized water and lyophilized in a vacuum freeze drier.

For comparison, MgAl-LDH with CO₃²⁻ intercalated in the interlayer (MgAl-LDH) was also fabricated by the same procedure except that solutions A and B were mixed dropwise in a reaction vessel without solution C. Pure MoS₂ was also prepared by hydrothermal processing. Na₂MoO₄·2H₂O (0.3 g) and thiourea (0.8 g) were dissolved in 65 mL degassed distilled water. The clear solution was aged for 24 h at 205 °C. Then, MoS₂ was washed several times with deionized water and lyophilized.

2.2. Characterization

The samples were characterized using X-ray diffraction (XRD, X'Pert PRO MRD), Raman spectroscopy (DXR Raman microscope), field emission scanning electron microscopy (FESEM, S-4800), high-resolution transmission electron microscopy (HRTEM, JEM-2100F), FTIR spectroscopy (Thermo Nicolet NEXUS 670), nitrogen adsorption-desorption experiments for surface and porosity quantification (NOVA-1200e) and X-ray photoelectron spectroscopy (XPS, ESCALAB 250Xi). The photoluminescence spectra of the materials were obtained with a fluorescence spectrophotometer (FluoroMax-4). The electrical behavior test was carried out using a semiconductor characterization system (4200-SCS). The degradation efficiency was determined by the concentration of MO studied by the spectrophotometer (UV-3600, Shimadzu). The mineralization

efficiency was measured by a Total Organic Carbon analyzer (multi N/C 3100).

2.3. Photocatalytic activity

The photocatalytic efficiency was measured by the degradation of methyl orange (MO) as a model contaminant. In general, 50 mg catalyst (1 g L⁻¹) was added to a 50 mL MO solution with a certain initial concentration (50, 100, 150 or 200 mg L⁻¹), and the pH of the solution was adjusted by 0.1 mol L⁻¹ HNO₃ or 1 mol L⁻¹ NaOH (pH = 3, 5, 7, 9 and 11). The mixture was stirred in the dark for 30 min to achieve adsorption/desorption equilibrium of MO with the catalyst. Then, the reaction system was exposed to light irradiation from a 500 W xenon lamp ($\lambda > 420$ nm) using a photochemical reaction apparatus (BL-GHX-V). During irradiation, 3 mL of the reaction solution was removed with a pipette at specific time intervals. The photocatalyst was removed from the solution *via* centrifugation. The MO concentration was measured by an ultraviolet-visible spectro-photometer at $\lambda = 464$ nm.

The degradation efficiency was calculated by the following formula:

$$\text{Degradation efficiency (\%)} = 100 \times (C_0 - C)/C_0 \quad (1)$$

where C_0 is the initial concentration of MO (mg L⁻¹) and C is the concentration of MO at another given irradiation time (mg L⁻¹). The mineralization efficiency was calculated by the following formula:

$$\text{Mineralization efficiency (\%)} = 100 \times (\text{TOC}_0 - \text{TOC})/\text{TOC}_0 \quad (2)$$

where TOC₀ is the initial total organic carbon of MO (mg L⁻¹) and TOC is the total organic carbon of MO at another given irradiation time (mg L⁻¹).

3. Results and discussion

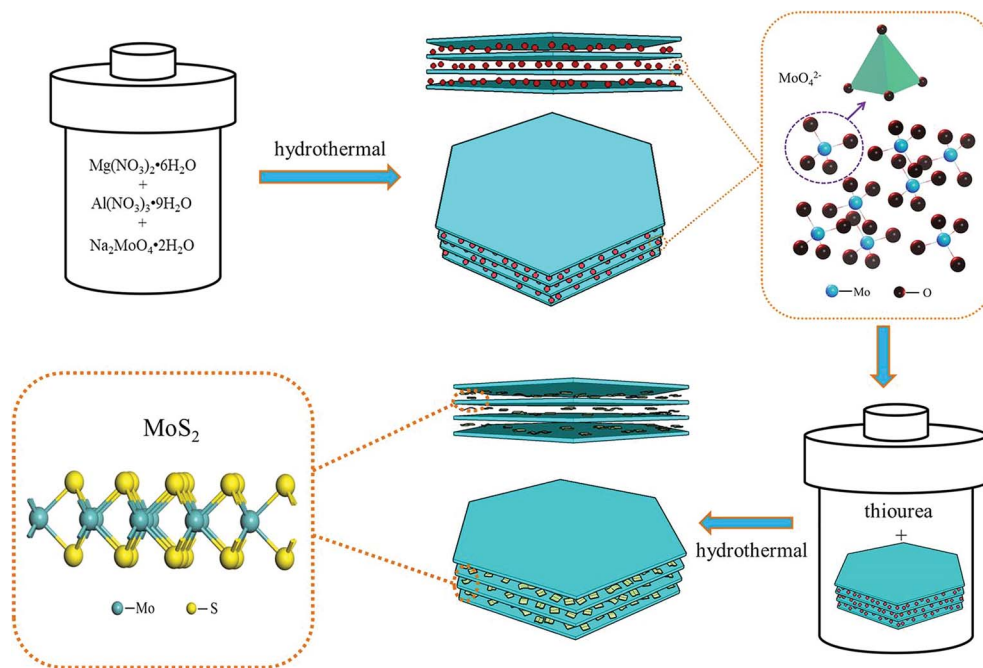
3.1. Structural design of the composite

The design of the MoS₂/MgAl-LDH composite is shown in Scheme 1. First, MoO₄²⁻ ions were added to the precursor solution of MgAl hydrotalcite. Due to the exchangeability of anions in the MgAl-LDH layers, MoO₄²⁻/MgAl-LDH was prepared by a hydrothermal method. Subsequently, MoO₄²⁻/MgAl-LDH was vulcanized in a hydrothermal process in a mild liquid phase environment. In this process, thiourea not only acts as a source of sulfur, but also releases H₂S as a protective atmosphere. In addition, in the liquid phase, it can improve the uniformity of the reaction sites of MoO₄²⁻ as well as acting as a sulfur source, which is beneficial to form few-layer MoS₂ in the MgAl-LDH layers.

3.2. Structural characterization of the composite

Fig. 1a shows the XRD patterns of MgAl-LDH, MoO₄²⁻/MgAl-LDH, MoS₂ and MoS₂/MgAl-LDH. The XRD pattern of MgAl-LDH has four diffraction peaks at 11.7°, 23.4°, 34.9° and 60.8°, which correspond to the (003), (006), (012) and (110) planes, respectively, of MgAl-LDH with the general formula





Scheme 1 Design of the MoS₂/MgAl-LDH growth process.

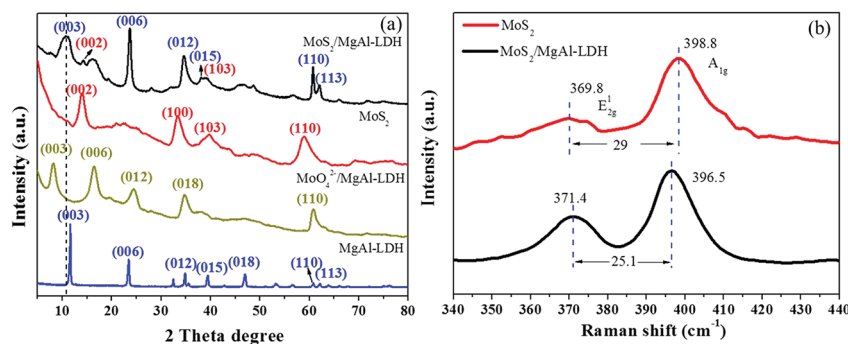


Fig. 1 XRD patterns of MgAl-LDH, MoO₄²⁻/MgAl-LDH, MoS₂ and MoS₂/MgAl-LDH (a), and Raman spectra of MoS₂ and MoS₂/MgAl-LDH (b).

(Mg_{0.667}Al_{0.333})(OH)₂(CO₃)_{0.167}(H₂O)_{0.5} (JPCDS no. 89-0460). The pristine MgAl-LDH pattern shows typical Bragg reflections of hexagonal LDH phases with interlayer carbonate anions. The MoO₄²⁻/MgAl-LDH composite has major diffraction peaks at 8.2°, 16.5°, 24.7° and 60.8°, which correspond to the (003), (006), (012) and (110) planes, respectively, of MgAl-LDH. The MoS₂/MgAl-LDH composite not only has major diffraction peaks at 10.65°, 23.4°, 34.9° and 60.8°, corresponding to the (003), (006), (012) and (110) planes of MgAl-LDH, but also has major diffraction peaks at 14.1° and 39.5°, which can be attributed to the (002) and (103) planes of MoS₂, respectively. In addition, the “a” value of the unit cell parameter did not change (as shown in Table 1). The unit cell parameters of LDHs correspond to the cation–cation distance in the brucite layer, which can be calculated by $a = 2 \times d(110)$. When MoO₄²⁻ and MoS₂ were inserted into MgAl-LDH, the substrate spacing increased from 7.6 Å to 10.8 Å and 8.3 Å, respectively. As shown in Scheme 2, the

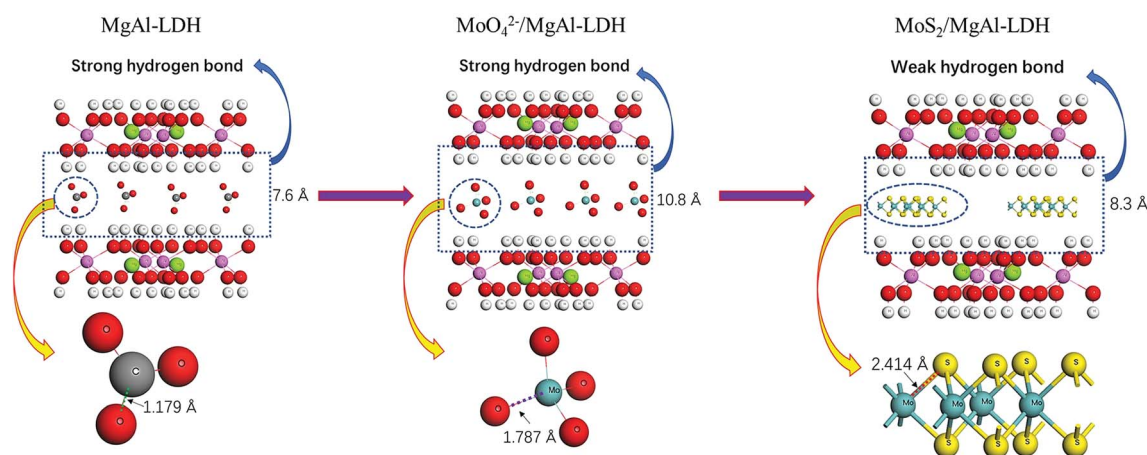
length of the C–O bond in the CO₃²⁻ anion is 1.179 Å in MgAl-LDH. When MoO₄²⁻ replaced the CO₃²⁻ anion in the MgAl-LDH layer, the spacing of the (003) plane increased from 7.6 Å to 10.8 Å. This is because the length of the Mo–O bond in the MoO₄²⁻ anion is 1.787 Å, which is larger than that of the C–O bond in the CO₃²⁻ ion. When MoS₂ was inserted into the LDH interlayer, the spacing of the (003) plane decreased to 8.3 Å, even though the length of the Mo–S bond was 2.414 Å. This is attributed to the weakening of the hydrogen bonding force between the MoS₂ compounds and the LDH layer. Fig. 1b shows the Raman spectra, which further reveal the microstructure of MoS₂ and MoS₂/MgAl-LDH. For MoS₂, two different Raman peaks at 369.8 and 398.8 cm⁻¹ are attributed to the typical E_{2g}¹ and A_{1g} modes of hexagonal MoS₂ crystals, respectively. In the case of MoS₂/MgAl-LDH, the two MoS₂ peaks are shifted to 371.4 and 396.5 cm⁻¹. Obviously, the frequency difference between the E_{2g}¹ and A_{1g} modes belonging to MoS₂ was 29 cm⁻¹, while for



Table 1 Structural characteristics of the samples obtained by hydrothermal synthesis^a

	MgAl-LDH	MoO ₄ ²⁻ /MgAl-LDH	MoS ₂ /MgAl-LDH	MoS ₂
<i>a</i> (Å)	3.05	3.05	3.05	—
<i>c</i> (Å)	22.8	32.4	24.9	—
<i>c'</i> (Å)	7.6	10.8	8.3	—
The thickness of the interlayer gallery ^b (Å)	2.8	6.0	3.5	—
Band gap (eV)	—	—	1.82	1.61

^a $a = 2d_{110}$, $c = 3d_{003}$ and $c = 3c'$. ^b The difference between c' and 4.8 Å (the thickness of the brucite-like sheet).¹⁶



Scheme 2 Schematic of the spacing change of the (003) plane.

MoS₂/MgAl-LDH this was reduced to 25.1 cm⁻¹. This confirms that the thickness of the MoS₂ nanosheets has been significantly reduced.³⁶

Fig. 2 shows the FTIR spectra of the various materials. As shown in Fig. 2a, strong and broad absorption bands at 3449, 3455 and 3449 cm⁻¹ are observed for MgAl-LDH, MoO₄²⁻/MgAl-LDH and MoS₂/MgAl-LDH, respectively. These can be attributed to the stretching vibration of the OH groups in the brucite-type layers and water molecules in the interlayer. The bands at 1618, 1635 and 1616 cm⁻¹ can be attributed to the bending vibration of interlayer water. The absorption bands at 3422 and 1624 cm⁻¹ for MoS₂ can be assigned to the stretching vibration

of the OH groups and the bending vibrations of water molecules adsorbed on the MoS₂ surface, respectively. Between 1000 and 400 cm⁻¹, the bands can be assigned to metal–oxygen (M–O) and metal–hydroxyl (M–OH) vibrations.^{17,18} The intense band characteristic of the ν_3 vibrations (antisymmetric stretching) of CO₃²⁻ ions located in the interlayer region can be observed at approximately 1360 cm⁻¹. The CO₃²⁻ peak intensities of MoS₂/MgAl-LDH and MoO₄²⁻/MgAl-LDH are much weaker than those of MgAl-LDH in the FTIR spectra. For MoO₄²⁻/MgAl-LDH, the antisymmetric stretching vibration band of Mo–O–Mo is observed at 820 cm⁻¹. The bands in the range of 400–1200 cm⁻¹ for MoS₂ and MoS₂/MgAl-LDH are shown in Fig. 2b. In the

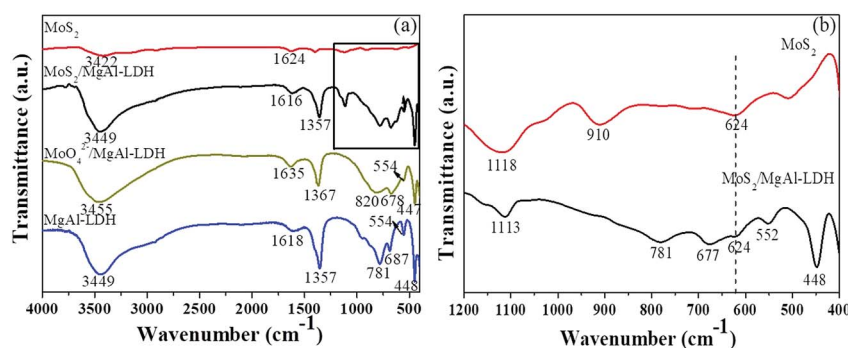


Fig. 2 FTIR spectra (a) of MgAl-LDH, MoS₂/MgAl-LDH and MoS₂ in the range of 400–4000 cm⁻¹; and (b) of MoS₂/MgAl-LDH and MoS₂ in the range of 400–1200 cm⁻¹.



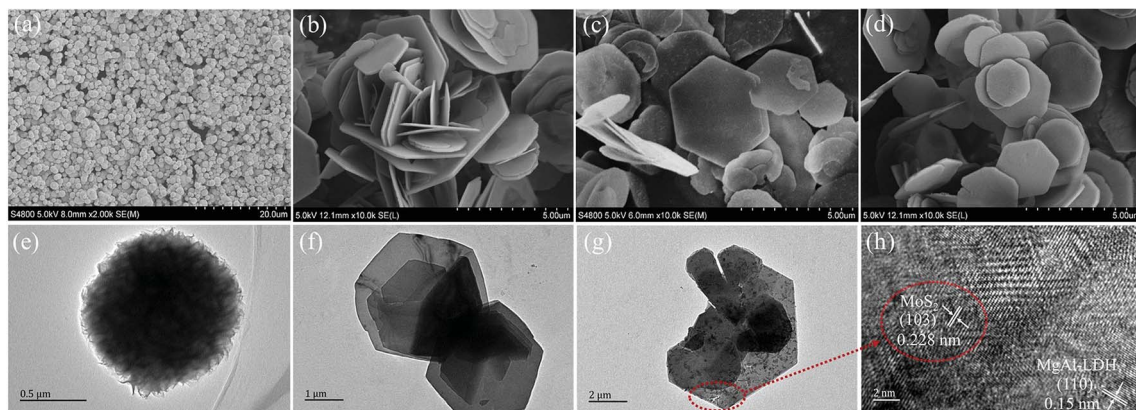


Fig. 3 FESEM images of MoS₂ (a), MgAl-LDH (b), MoO₄²⁻/MgAl-LDH (c), and MoS₂/MgAl-LDH (d). TEM images of MoS₂ (e), MgAl-LDH (f), and MoS₂/MgAl-LDH (g) and HRTEM image of MgAl-LDH (h).

spectrum of MoS₂, the peak at 910 cm⁻¹ can be attributed to the Mo=O stretching vibration, which may be caused by the formation of a small amount of oxide on the MoS₂ surface. The peaks at 1113 and 1118 cm⁻¹ for MoS₂/MgAl-LDH and MoS₂, respectively, can be attributed to the S=O asymmetric stretching vibration. In the spectra of MoS₂/MgAl-LDH and MoS₂, the peak at 624 cm⁻¹ can be assigned to the Mo-S stretching vibration.

Typical FESEM images of the samples are shown in Fig. 3a–d. As shown in Fig. 3a, the morphology of pure MoS₂ is flower-like. Moreover, each MoS₂ microsphere has an average diameter of approximately 1 μm. Fig. 3b–d show the morphology of MgAl-LDH, MoO₄²⁻/MgAl-LDH and MoS₂/MgAl-LDH, respectively. It can be observed that all the samples maintain a hexagonal-like sheet structure. As shown in Fig. 3d, we didn't find any particles with a similar morphology to pure MoS₂ in the MoS₂/MgAl-LDH composite. This indicates that the morphology of MgAl-LDH has not changed after ion exchange and vulcanization. The microstructures of the samples were investigated through TEM (Fig. 3e–g) and HRTEM (Fig. 3h). Fig. 3e shows MoS₂ samples displaying flower-like spherical structures with diameters of 1–1.2 μm and Fig. 3f shows that MgAl-LDH is a highly dispersed flake. Interestingly, as shown in Fig. 3g, it is clearly shown that the MoS₂ nanosheet exhibits an irregular sheet-like structure in the layers of MgAl-LDH, and MgAl-LDH is decorated by MoS₂ and serves as a carrier. Moreover, the HRTEM image of MoS₂/MgAl-LDH is shown in Fig. 3h. The interplanar spacings of 0.228 and 0.15 nm can be attributed to the (103) and (110) planes of MoS₂ and MgAl-LDH, respectively. This also indicates that MoS₂ was successfully grown between the MgAl-LDH layers.

To verify the interfacial nature of MoS₂ and MgAl-LDH in the MoS₂/MgAl-LDH sample, XPS measurements were carried out. As shown in Fig. 4a, the XPS spectra of MoS₂/MgAl-LDH show Al 2p, S 2p, Mo 3d, C 1s, O 1s and Mg 1s binding energy peaks at 73.8 eV, 160.2 eV, 227.2 eV, 284.6 eV, 531.4 eV and 1303.7 eV, respectively. As shown in Fig. 4b, two peaks were observed at 228.3 and 231.6 eV, which could be attributed to Mo 3d_{5/2} and Mo 3d_{3/2} binding energies, respectively,^{19,20} and are the characteristic peaks of Mo⁴⁺ in MoS₂. Two peaks at 232.5 and

235.7 eV are related to the Mo 3d_{5/2} and 3d_{3/2} binding energies of Mo⁶⁺, respectively.¹⁶ The small peak at 225.6 eV corresponds to the S 2s binding energy of MoS₂.¹⁶ The S spectrum is shown in Fig. 4c. Two main peaks at 160.2 and 161.3 eV can be assigned to the S 2p_{3/2} and S 2p_{1/2} lines of MoS₂, respectively. The small peak at 167.5 eV suggests the existence of bridging disulfides S⁴⁺.²² As illustrated in Fig. 4d, the C 1s spectrum can be decomposed into a dominant peak at 284.6 eV for C=C/C-C²³ and a weak peak at 288.5 eV for C=O in oxygen-containing functional groups. The XPS results show that there is no chemical bond between MoS₂ and MgAl-LDH in the MoS₂/MgAl-LDH catalyst.

The XRD, FTIR, FESEM, HRTEM and XPS analysis showed that few-layer MoS₂ was successfully prepared in the MgAl-LDH layers by the hydrothermal method, which takes advantage of the “space-confining” effect of MgAl-LDH. Therefore, the synthetic design was reasonable *via* Scheme 1.

3.3. Photocatalytic performance

To better understand the photocatalytic performance of the MoS₂/MgAl-LDH composite, different solution pH values were used for the photodegradation of MO, as shown in Fig. 5a. The degradation rate of MoS₂/MgAl-LDH was the lowest at pH = 11, with only 19.23% of the MO degraded after 120 min. The photocatalytic ability of the sample increased as the pH decreased, and the degradation rate reached its highest at pH = 3, implying that the optimal photocatalytic capacity of MoS₂/MgAl-LDH occurred under acidic conditions. Fig. 5b compares the degradation rate and mineralization rate of MO under different pH values under visible light irradiation for 2 h. The degradation efficiency and mineralization efficiency of MO without the catalyst were only 0.48% and 0.09% respectively, which indicates that the MO molecule and intermediate products were difficult to self-degrade. When the MO solution pH = 3, the degradation efficiency and mineralization efficiency achieved 84.88% and 73.25%, respectively. Therefore, the optimal condition in this study was pH = 3.

The degradation rate using MoS₂/MgAl-LDH for different concentrations of MO is shown in Fig. 5c. The MO solution



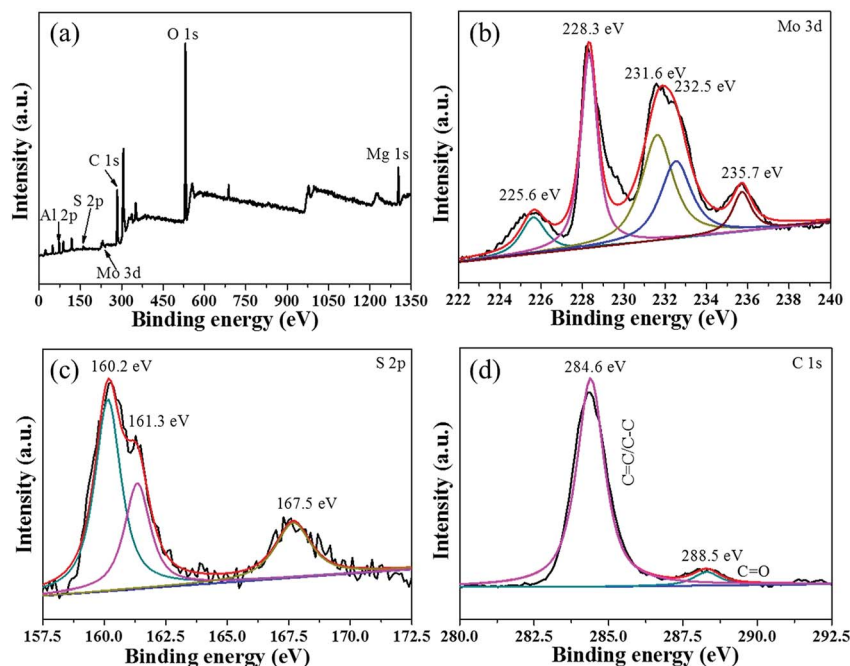


Fig. 4 XPS spectra of the MoS₂/MgAl-LDH sample (a) and high-resolution XPS spectra of Mo 3d (b), S 2p (c), and C 1s (d).

concentrations were 50, 100, 150 and 200 mg L⁻¹. As shown in Fig. 5c, the MO solutions with initial concentrations of 50 mg L⁻¹ and 100 mg L⁻¹ were completely degraded after reacting for 45 min and 105 min, respectively. In addition, the degradation efficiency was over 84% after 120 min when the initial concentrations of MO were 150 mg L⁻¹ and 200 mg L⁻¹. In addition, the mineralization efficiency of MO (Fig. 5d) at initial concentrations of 50 mg L⁻¹, 100 mg L⁻¹, 150 mg L⁻¹ and 200 mg L⁻¹ achieved 97.25%, 96.74%, 79.56% and 73.25%, respectively. Compared with other catalysts (in Table 2), MoS₂/MgAl-LDH exhibited excellent catalytic performance at high concentrations of MO. To better verify the catalytic effect of the catalyst, a methyl orange concentration of 200 mg L⁻¹ was selected for subsequent tests.

For comparison, pure MoS₂ and MgAl-LDH were also tested under the same conditions. The photocatalytic performances of the samples under visible-light irradiation are shown in Fig. 5e and f. The degradation efficiency and mineralization efficiency were 38.66% and 10.25% for MoS₂, 16.57% and 2.73% for MgAl-LDH, respectively. These are lower than the values (84.88% and 73.25%) for MoS₂/MgAl-LDH, indicating that the synergistic effect between MoS₂ and MgAl-LDH enhanced the catalytic activity.

Fig. 5g shows the MO kinetic analysis with MoS₂, MgAl-LDH and MoS₂/MgAl-LDH. The kinetics of photocatalytic reactions of organic pollutants are usually described by the Langmuir-Hinshelwood model. The photocatalytic process of MO can be expressed by the following pseudo first-order kinetic equation:²⁶

$$-\ln\left(\frac{C_t}{C_0}\right) = K_{app}t \quad (3)$$

$$t_{1/2} = \frac{\ln 2}{K_{app}} \quad (4)$$

where C_0 and C_t are the initial MO concentration and the concentration at time t , respectively, and K_{app} is the photocatalytic reaction rate constant (min⁻¹). The K_{app} , linearization coefficient (R^2) and half-life ($t_{1/2}$) are given in Table 3. The high value of the linear regression coefficient (R^2) indicates that the photocatalytic reaction is well matched to the pseudo first-order kinetic model. MoS₂/MgAl-LDH showed the best photocatalytic performance, which was indicated by the largest value of K_{app} . The catalytic cycling performance of MoS₂/MgAl-LDH was investigated by reusing it four consecutive times as shown in Fig. 5h, and the degradation rate of MO was still above 80% after four cycles. This shows that the MoS₂/MgAl-LDH catalyst has excellent catalytic performance and reusability, even with a MO concentration as high as 200 mg L⁻¹. Fig. 5i shows the FTIR spectra of MoS₂/MgAl-LDH before and after photocatalysis. After photocatalysis, no characteristic peak of MO appeared in the FTIR spectra, proving that MoS₂/MgAl-LDH acts on MO *via* photocatalysis instead of adsorption.

3.4. The mechanism of the improvement in photocatalytic performance for MoS₂/MgAl-LDH

Fig. 6a and b show the nitrogen adsorption-desorption isotherms and corresponding BJH pore size distributions, respectively, of MoS₂, MgAl-LDH and MoS₂/MgAl-LDH. The isotherms are IV isotherms with H3 hysteresis loops, indicating porous flat agglomerates or lamellar particles.³⁷ The calculated BET surface area was 14.06 m² g⁻¹ for MgAl-LDH, 13.18 m² g⁻¹ for MoS₂, and 9.83 m² g⁻¹ for MoS₂/MgAl-LDH. The results demonstrate that the excellent photocatalytic performance of



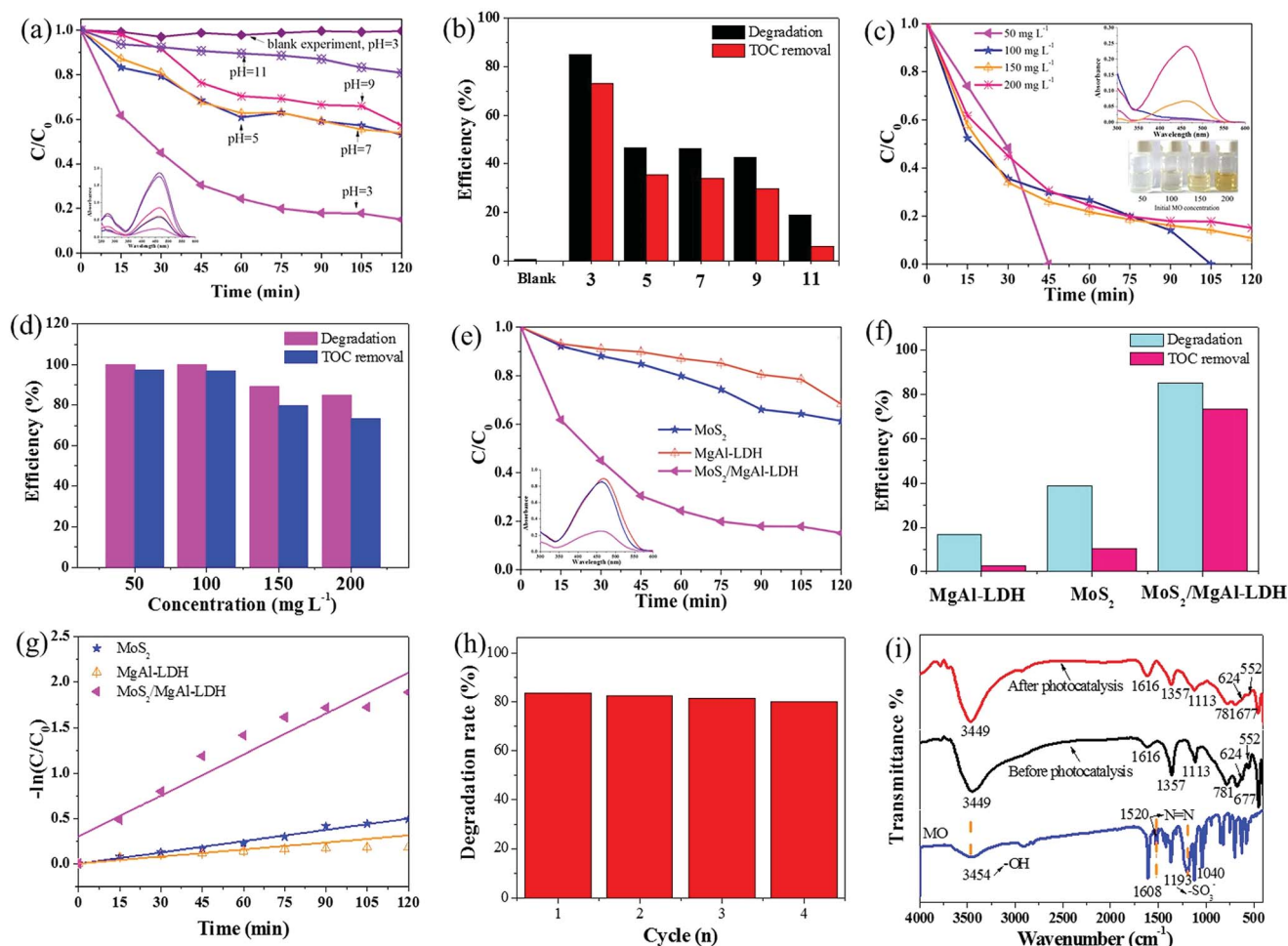


Fig. 5 Effect of initial solution pH values on the photodegradation (a) and mineralization (b) of MO (conditions: initial MO concentration 200 mg L^{-1} , photocatalyst dosage 1 g L^{-1}). Inset: UV-vis spectra of catalyzed solutions. Effect of initial MO concentration on the photodegradation (c) and mineralization (d) of MO (conditions: initial solution pH = 3, adsorbent dosage 1 g L^{-1}). Inset: the UV-vis spectra of catalyzed solutions (top) and optical photographs of supernatants obtained by centrifugation (bottom). Photocatalytic degradation curves (e) and mineralization efficiency (f) of the samples. Inset: the UV-vis spectra of catalyzed solutions. The kinetic analysis of the samples (g). Cycles of photocatalytic degradation of MO using $\text{MoS}_2/\text{MgAl-LDH}$ (h) and FTIR spectra of $\text{MoS}_2/\text{MgAl-LDH}$ before and after photocatalysis (i).

$\text{MoS}_2/\text{MgAl-LDH}$ does not depend on the specific surface area. As shown in Fig. 6c, compared with that of pure MoS_2 and MgAl-LDH , the absorbance of $\text{MoS}_2/\text{MgAl-LDH}$ in the visible region is enhanced. The enhanced absorption of $\text{MoS}_2/\text{MgAl-LDH}$ will yield more photons to produce more photogenerated carriers, which could enhance the photocatalytic activity. The optical

band gaps of the prepared photocatalysts were determined by the following equation ($\alpha = A(h\nu - E_g)^{n/2}/h\nu$).³⁸ As shown in Fig. 6d and e, the bandgap of MoS_2 increases from 1.62 to 1.78 eV, which is due to the decreasing domain size of MoS_2 grown in the MgAl-LDH layers. The recombination distance of electron-hole pairs is increased with the increased band gap of MoS_2 .

Table 2 The photocatalytic activity of several photocatalysts for MO

Photocatalyst	MO concentration	Photocatalyst dosage	Results	References
$\text{TiO}_2/\text{MoS}_2@\text{zeolite}$	20 mg L^{-1}	0.5 g L^{-1}	Removal of 100% in 60 min	30
Ag/TiO_2	$5 \times 10^{-5} \text{ M}$ (16.3 mg L^{-1})	1 g L^{-1}	Removal of 100% in 80 min	31
$\text{MoS}_2/\text{YVO}_4$	10 mg L^{-1}	1 g L^{-1}	Removal of 100% in 30 min	32
$\text{Cu}_2\text{O}/\text{ZnAl-CLDH}$	20 mg L^{-1}	1 g L^{-1}	Removal of approximately 90% in 420 min	33
$\text{TiO}_2/\text{biochar}$	20 mg L^{-1}	0.25 g L^{-1}	Removal of 100% in 150 min	34
$\text{MoS}_2/\text{MgAl-LDH}$	50 mg L^{-1}	1 g L^{-1}	Removal of 100% in 45 min	This work
	100 mg L^{-1}	1 g L^{-1}	Removal of 100% in 105 min	
	200 mg L^{-1}	1 g L^{-1}	Removal of approximately 84% in 120 min	



Table 3 Parameters of the pseudo first-order kinetic model for photocatalytic degradation

Photocatalysts	K_{app} (min^{-1})	R^2	$t_{1/2}$ (min)
MoS ₂	0.00416	0.9832	166.59
MgAl-LDH	0.00259	0.89659	267.62
MoS ₂ /MgAl-LDH	0.01505	0.90051	46.06

To verify the synergistic mechanism between MoS₂ and MgAl-LDH in MoS₂/MgAl-LDH, photoluminescence (PL) measurements of the samples were also carried out. The PL spectra of the samples in the range $\lambda = 265\text{--}330$ nm with an excitation wavelength of 250 nm are shown in Fig. 6f. These materials exhibited a strong PL emission peak at $\lambda \approx 290$ nm due to charge carrier capture on the surface.²⁷ Compared with that of pure MoS₂ and MgAl-LDH, the PL signal of MoS₂/MgAl-LDH was the weakest, which indicated the sample had the lowest photogenerated electron-hole pair recombination rate²⁸ and the highest electron-hole pair separation efficiency. Obviously, the recombination efficiency of electron-hole pairs was inhibited in MgAl-LDH when MoS₂ grew in the MgAl-LDH layers.

Usually, nano-sized noble metals are used to modify the surfaces of semiconductors to form metal-semiconductor junctions to enhance electron-hole separation.³⁹ However, there is no metal-semiconductor junction found in MoS₂/MgAl-LDH composites, which can be confirmed by the above XPS results. Semiconductor testing is used to investigate the electrical behavior of the sample, as shown in Fig. 7. The samples

were prepared into wafers 10 mm in diameter and 0.2 mm in thickness. Fig. 7a–c show the resistance tests of MgAl-LDH (Fig. 7a), MoS₂ (Fig. 7b) and MoS₂/MgAl-LDH (Fig. 7c), respectively. It can be clearly observed that the resistance meter of MgAl-LDH showed “O.L”, indicating that the sample was nonconducting. Interestingly, the resistance of MoS₂ varied from 1.52 to “O.L”, and the resistance of MoS₂/MgAl-LDH varied from 8.74 to “O.L”. To better analyze the semiconductor characteristics of MoS₂ and MoS₂/MgAl-LDH, the samples were tested using a semiconductor characteristic system. Fig. 7d and e showed obvious semiconductor characteristic curves, indicating similar semiconductor properties between MoS₂/MgAl-LDH and MoS₂. It was likely that MgAl-LDH played the role of conductive layer in MoS₂/MgAl-LDH.

In addition, the effect of different capture agents on the photocatalytic activity of MoS₂/MgAl-LDH is shown in Fig. 8. The scavengers of O₂^{•−}, h⁺ and OH[•] were benzoquinone (BQ), ethylenediaminetetraacetic acid (Na₂-EDTA) and isopropanol (IPA), respectively. It is shown that adding IPA significantly inhibited MO degradation, indicating that OH[•] was one of the important active species in the photodegradation process. Likewise, the degradation ability of the composite is inhibited with the addition of Na₂-EDTA and BQ. Therefore, h⁺ and O₂^{•−} are also major active species. In summary, OH[•], h⁺ and O₂^{•−} are the major active species for catalyzing MO in MoS₂/MgAl-LDH.

Based on the above discussion, the mechanism of the improvement in photocatalytic performance of MoS₂/MgAl-LDH is revealed in Scheme 3. On the one hand, few-layer MoS₂ nanosheets were prepared by the “space-confining” effect of MgAl-LDH. The bandgap of MoS₂ is increased from

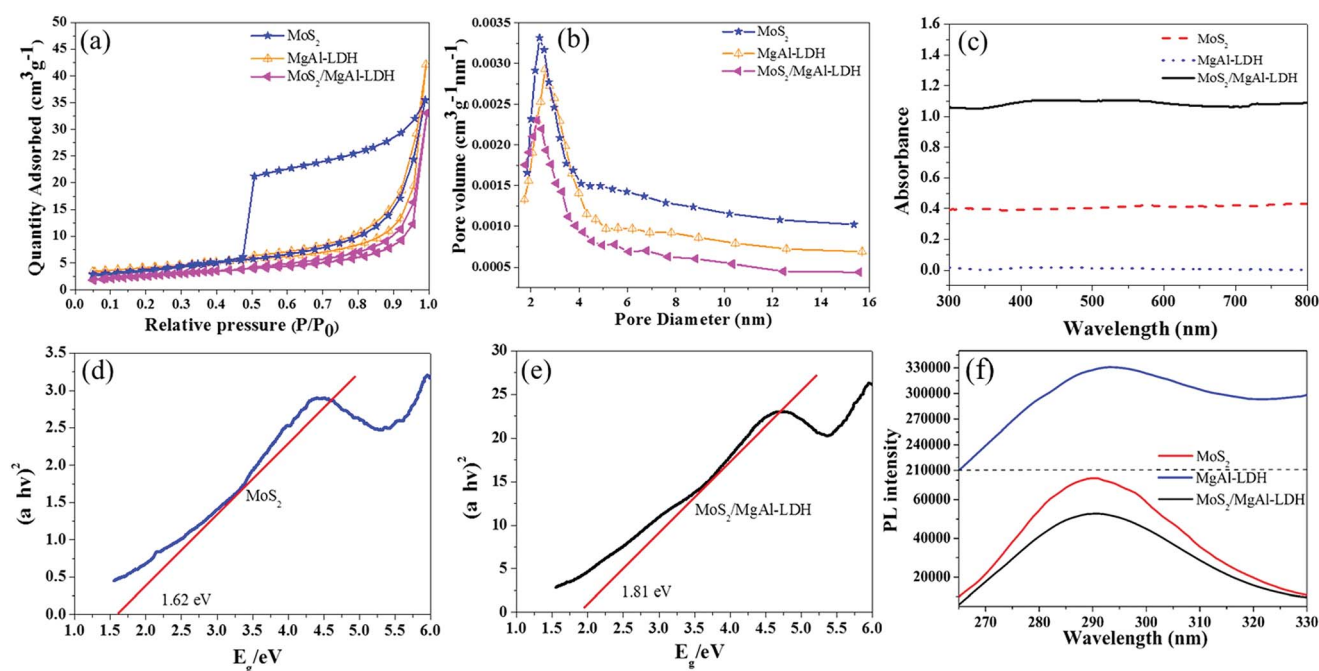


Fig. 6 N₂ adsorption–desorption isotherm curves (a) and pore size distribution curves (b) of the samples. UV-vis spectra of MgAl-LDH, MoS₂ and MoS₂/MgAl-LDH (c) and the bandgap curves of MoS₂ (d) and MoS₂/MgAl-LDH (e). Fluorescence spectra of MgAl-LDH, MoS₂ and MoS₂/MgAl-LDH (f).



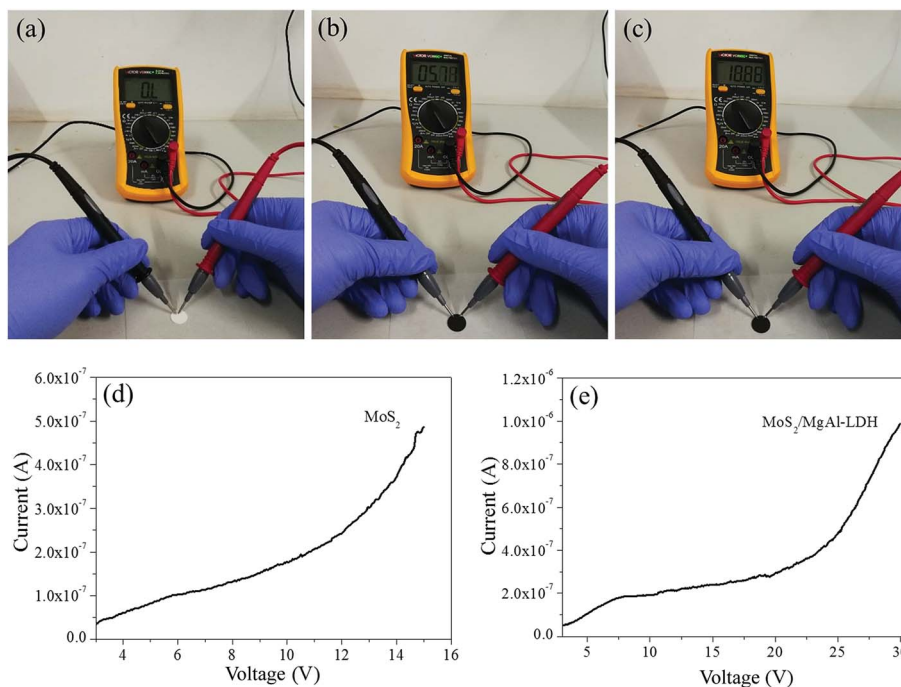


Fig. 7 Electrical characteristics of MgAl-LDH (a), MoS₂ (b), and MoS₂/MgAl-LDH (c). Semiconductor characteristic curves of MoS₂ (d), and MoS₂/MgAl-LDH (e).

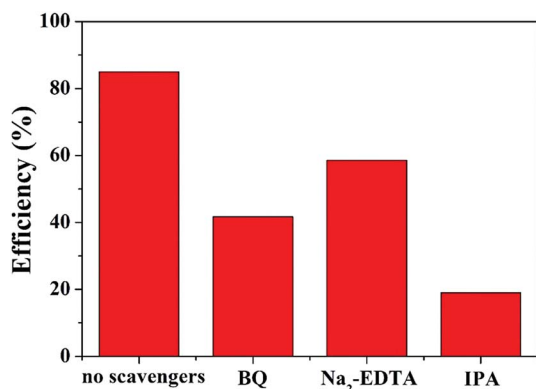
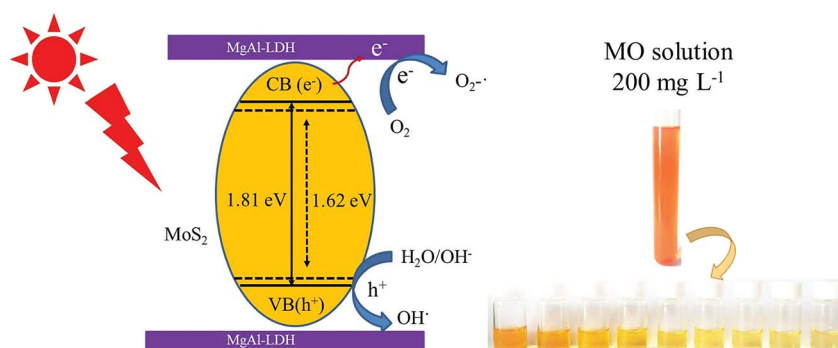


Fig. 8 Photocatalysis tests with different quenchers over MoS₂/MgAl-LDH.

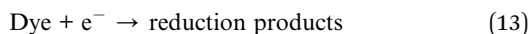
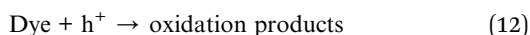
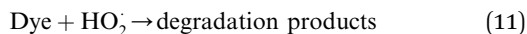
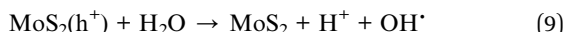
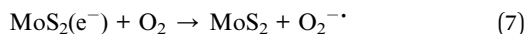
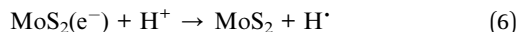
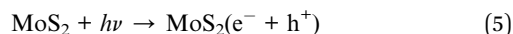
1.62 to 1.81 eV due to the quantum limitation effect, leading the photogenerated electron-hole pairs having a stronger redox ability. On the other hand, the MgAl-LDH layer acts as an inorganic conductive layer, which could rapidly transfer photogenerated electrons from MoS₂, thus inhibiting the recombination of photogenerated electron-hole pairs. Moreover, a possible photocatalytic degradation mechanism can be proposed. First, the MO molecules are adsorbed in a layer on MoS₂/MgAl-LDH due to the charge on the surface of MgAl-LDH. Meanwhile, under visible light, photoelectrons and holes are generated in the conduction and valence bands, respectively, of MoS₂. Then, the photogenerated electrons transferred to the MgAl-LDH layer react with oxygen adsorbed on the surface or dissolved in water to produce superoxide. The excess holes on the valence band remain in MoS₂ and react with H₂O and OH⁻



Scheme 3 Photocatalytic mechanism schematic of MO degradation by MoS₂/MgAl-LDH.



to form active substances such as OH^\cdot .²⁹ Then, photocatalysis proceeds by a known mechanism of visible-light-driven electron emission from the valence band to the conduction band, and the formation of oxidative intermediate species, $\text{O}_2^{\cdot-}$ and OH^\cdot , results in the degradation of MO.



4. Conclusions

In summary, few-layer MoS_2 was successfully grown in MgAl-LDH layers. By decreasing the domain size of MoS_2 , the bandgap of MoS_2 was increased from 1.62 eV (flower-like MoS_2) to 1.81 eV ($\text{MoS}_2/\text{MgAl-LDH}$), and the $\text{MoS}_2/\text{MgAl-LDH}$ composite exhibits a significantly enhanced full-spectrum response in the wavelength range of 300–800 nm. More importantly, the MgAl-LDH layer acts as an inorganic conductive layer to transport photogenerated electrons efficiently. As a result, there is a lower recombination efficiency of photo-generated electron-hole pairs in the $\text{MoS}_2/\text{MgAl-LDH}$ composite. Therefore, the $\text{MoS}_2/\text{MgAl-LDH}$ composite exhibited an outstanding catalytic capacity and a superior cycle performance. The composite completely degraded the MO in 50 mg L^{-1} and 100 mg L^{-1} MO solutions in 45 min and 105 min, respectively. Furthermore, the composite also shows a degradation rate over 84% in 120 min even for a MO solution concentration as high as 200 mg L^{-1} , and retained 80% of the initial degradation rate after four cycles. The $\text{MoS}_2/\text{MgAl-LDH}$ composite can be considered as a promising photocatalyst for waste water treatment.

Conflicts of interest

There are no conflicts to declare.

Acknowledgements

We acknowledge the financial support from the National Natural Science Foundation of China (No. 51672052), Guangxi Distinguished Experts Special Fund (2015B017), Guangxi

Graduate Education Innovation Program and Improving the Basic Ability of Young and Middle-aged University Teachers in Guangxi (No. KY2018KY0256).

References

- 1 K. Iqbal, A. Iqbal, A. M. Kirillov, B. Wang, W. Liu and Y. Tang, *J. Mater. Chem. A*, 2017, **5**, 6716–6724.
- 2 J. S. Valentea, F. Tzompantzi and J. Princec, *Appl. Catal., B*, 2011, **102**, 276–285.
- 3 X. Liu, X. Zhao, Y. Zhu and F. Zhang, *Appl. Catal., B*, 2013, **140**, 241–248.
- 4 V. K. Gupta and T. A. Saleh, *Environ. Sci. Pollut. Res. Int.*, 2013, **20**, 2828–2843.
- 5 O. Legrini, E. Oliveros and A. M. Braun, *Chem. Rev.*, 1993, **93**, 671–698.
- 6 H. Li, J. Li, C. Xu, P. Yang, D. H. L. Ng, P. Song and M. Zuo, *J. Alloys Compd.*, 2017, **698**, 852–862.
- 7 J. Cha, K. Koski, K. Huang, K. Wang, W. Luo and D. Kong, *Nano Lett.*, 2013, **13**, 5913–5918.
- 8 K. Wang, J. Wang, J. Fan, M. Lotya, A. O'Neill, D. Fox, Y. Feng, X. Zhang, B. Jiang, Q. Zhao, H. Zhao, J. Coleman, L. Zhang and W. Blau, *ACS Nano*, 2013, **7**, 9260–9267.
- 9 Y. Li, Y. Rao, K. F. Mak, Y. You, S. Wang, C. R. Dean and T. F. Heinz, *Nano Lett.*, 2013, **13**, 3329–3333.
- 10 T. Li and G. Galli, *J. Phys. Chem. C*, 2007, **111**, 16192–16196.
- 11 A. Splendiani, L. Sun, Y. Zhang, T. Li, J. Kim, C. Y. Chim, G. Galli and F. Wang, *Nano Lett.*, 2010, **10**, 1271–1275.
- 12 M. Lotya, Y. Hernandez, P. J. King, R. J. Smith, V. Nicolosi, L. S. Karlsson, F. M. Blighe, S. De, Z. Wang, I. T. McGovern, G. S. Duesberg and J. N. Coleman, *J. Am. Chem. Soc.*, 2009, **131**, 3611–3620.
- 13 M. Lotya, P. J. King, U. Khan, S. De and J. N. Coleman, *ACS Nano*, 2010, **4**, 3155–3162.
- 14 R. J. Smith, P. J. King, M. Lotya, C. Wirtz, U. Khan, S. De, A. O'Neill, G. S. Duesberg, J. C. Grunlan, G. Moriarty, J. Chen, J. Wang, A. I. Minett, V. Nicolosi and J. N. Coleman, *Adv. Mater.*, 2011, **23**, 3944–3948.
- 15 M. D. J. Quinn, N. H. Ho and S. M. Notley, *ACS Appl. Mater. Interfaces*, 2013, **5**, 12751–12756.
- 16 M. Li, L. Zhang, X. Fan, M. Wu, Y. Du, M. Wang, Q. Kong, L. Zhang and J. Shi, *Appl. Catal., B*, 2016, **190**, 36–43.
- 17 S. Mancipe, F. Tzompantzi and R. Gómez, *Appl. Clay Sci.*, 2017, **136**, 67–74.
- 18 P. Kuśtrowski, A. Rafalska-Łasocha, D. Majda, D. Tomaszewska and R. Dziembaj, *Solid State Ionics*, 2001, **141**, 237–242.
- 19 Y. Shi, Y. Wang, J. I. Wong, A. Y. S. Tan, C. L. Hsu, L. J. Li, Y. C. Lu and H. Y. Yang, *Sci. Rep.*, 2013, **3**, 2169.
- 20 Y. Sun, X. Hu, W. Luo and Y. Huang, *J. Mater. Chem.*, 2011, **22**, 425–431.
- 21 Y. Zhang, N. Afzal, L. Pan, X. Zhang and J. Zou, *Adv. Sci.*, 2019, **6**, 1900053–1900072.
- 22 V. O. Koroteev, L. G. Bulusheva, I. P. Asanov, E. V. Shlyakhova, D. V. Vyalikh and A. V. Okotrub, *J. Phys. Chem. C*, 2011, **115**, 21199–21204.



- 23 Y. Teng, H. Zhao, Z. Zhang, Z. Li, Q. Xia, Y. Zhang, L. Zhao, X. Du, Z. Du and P. Lv, *ACS Nano*, 2016, **10**, 8526–8535.
- 24 G. Shen, L. Pan, Z. Lü, C. Wang, F. Aleem, X. Zhang and J. Zou, *Chin. J. Catal.*, 2018, **39**, 920–928.
- 25 Z. Lv, N. Mahmood, M. Tahir, L. Pan, X. Zhang and J. Zou, *Nanoscale*, 2016, **8**, 18250–18269.
- 26 Y. Zhou, L. Shuai, X. Jiang, F. Jiao and J. Yu, *Adv. Powder Technol.*, 2015, **26**, 439–447.
- 27 C. Y. Lin, Y. C. Wang, S. J. Hsu, C. F. Lo and W. G. Diao, *J. Phys. Chem. C*, 2010, **114**, 176–184.
- 28 X. Liu, L. Pan, Q. Zhao, T. Lv, G. Zhu, T. Chen, T. Lu, Z. Sun and C. Sun, *Chem. Eng. J.*, 2012, **183**, 238–243.
- 29 M. O. Ansari, M. M. Khan, S. A. Ansari, I. Amal, J. Lee and M. H. Cho, *Mater. Lett.*, 2014, **114**, 159–162.
- 30 W. Zhang, X. Xiao, L. Zheng and C. Wan, *Appl. Surf. Sci.*, 2015, **358**, 468–478.
- 31 R. Saravanan, D. Manoj, J. Qin, M. Naushad, F. Gracia, A. F. Lee, M. M. Khan and M. A. G. Pinilla, *Process Saf. Environ. Prot.*, 2018, **120**, 339–347.
- 32 Q. Chen, C. Zhao, Y. Wang, Y. Chen, Y. Ma, Z. Chen, J. Yu, Y. Wu and Y. He, *Sol. Energy*, 2018, **171**, 426–434.
- 33 X. Wu, D. Zhang, F. Jiao and S. Wang, *Colloids Surf., A*, 2016, **508**, 110–116.
- 34 L. Lu, R. Shan, Y. Shi, S. Wang and H. Yuan, *Chemosphere*, 2019, **222**, 391–398.
- 35 P. Šárka, J. Krýsa, J. Jirkovský, F. Claude, M. Gilles and P. Vanessa, *Appl. Catal., B*, 2015, **170–171**, 25–33.
- 36 C. Lee, H. Yan, L. E. Brus, T. F. Heinz, J. Hone and S. Ryu, *ACS Nano*, 2010, **4**, 2695–2700.
- 37 S. Mancipe, F. Tzompantzi and R. Gómez, *React. Kinet., Mech. Catal.*, 2017, **122**, 625–634.
- 38 D. S. Ginley and M. A. Butler, *J. Appl. Phys.*, 1977, **48**, 2019–2021.
- 39 C. Liu, D. Kong, P. C. Hsu, H. Yuan, H. W. Lee, Y. Liu, H. Wang, S. Wang, K. Yan, D. Lin, P. A. Maraccini, K. M. Parker, A. B. Boehm and Y. Cui, *Nat. Nanotechnol.*, 2016, **11**, 1098–1104.

